

# Ground-state properties of super-heavy hydrogen-7

**Manuel Caamano** (✉ [manuel.fresco@usc.es](mailto:manuel.fresco@usc.es))

University of Santiago de Compostela <https://orcid.org/0000-0002-5045-003X>

**thomas roger**

GANIL

**Antonio Moro**

University of Sevilla

**Gwen Grinyer**

University of Regina <https://orcid.org/0000-0001-6407-7064>

**Julien Pancin**

GANIL, CEA/DSM-CNRS/IN2P3

**Soumya Bagchi**

GSI Helmholtzzentrum für Schwerionenforschung <https://orcid.org/0000-0001-9934-1902>

**Sara Sambi**

KU Leuven

**Julien Gibelin**

LPC Caen, University of Caen <https://orcid.org/0000-0001-6751-3714>

**Beatriz Fernández-Domínguez**

University of Santiago de Compostela

**Naoyu Itagaki**

University of Tokyo

**Jose Benlliure**

University of Santiago de Compostela

**Dolores Cortina**

University of Santiago de Compostela

**Fanny Farget**

LPC Caen, University of Caen

**Bertrand Jacquot**

GANIL, CEA/DSM-CNRS/IN2P3

**David Pérez-Loureiro**

Canadian Nuclear Laboratories <https://orcid.org/0000-0002-0609-1308>

**Benjamim Pietras**

University of Santiago de Compostela

**Riccardo Raabe**

Instituut voor Kernfysica, KU Leuven

**Diego Ramos**

GANIL, CEA/DSM–CNRS/IN2P3

**Carne Rodríguez-Tajes**

GANIL, CEA/DSM–CNRS/IN2P3

**Herve Savajols**

GANIL, CEA/DSM–CNRS/IN2P3

**Marine Vandebrouck**

CEA, University of Paris-Saclay

---

**Article**

**Keywords:**

**Posted Date:** November 9th, 2020

**DOI:** <https://doi.org/10.21203/rs.3.rs-94738/v1>

**License:**  This work is licensed under a Creative Commons Attribution 4.0 International License.

[Read Full License](#)

---

# Ground-state properties of super-heavy hydrogen-7

M. Caamaño,<sup>1,\*</sup> T. Roger,<sup>2,†</sup> A. M. Moro,<sup>3</sup> G. F. Grinyer,<sup>2,‡</sup> J. Pascin,<sup>2</sup> S. Bagchi,<sup>4,§</sup>  
S. Sambhi,<sup>5</sup> J. Gibelin,<sup>6</sup> B. Fernández-Domínguez,<sup>1</sup> N. Itagaki,<sup>7</sup> J. Benlliure,<sup>1</sup>  
D. Cortina-Gil,<sup>1</sup> F. Farget,<sup>2,¶</sup> B. Jacquot,<sup>2</sup> D. Pérez-Loureiro,<sup>2,\*\*</sup> B. Pietras,<sup>1</sup>  
R. Raabe,<sup>5</sup> D. Ramos,<sup>1,††</sup> C. Rodríguez Tajés,<sup>2</sup> H. Savajols,<sup>2</sup> and M. Vandebrouck<sup>8,‡‡</sup>

<sup>1</sup>*IGFAE – Universidad de Santiago de Compostela, E-15706 Santiago de Compostela, Spain*

<sup>2</sup>*GANIL, CEA/DSM–CNRS/IN2P3, BP 55027, F-14076 Caen Cedex 5, France*

<sup>3</sup>*Universidad de Sevilla, E-41080 Sevilla, Spain*

<sup>4</sup>*KVI-CART, University of Groningen, NL-9747 AA, Groningen, The Netherlands*

<sup>5</sup>*Instituut voor Kernfysica, KU Leuven, B-3001 Leuven, Belgium*

<sup>6</sup>*LPC Caen, Université de Caen Basse-Normandie–ENSICAEN–CNRS/IN2P3, F-14050 Caen Cedex, France*

<sup>7</sup>*Yukawa Institute for Theoretical Physics, Kyoto University,*

*Kitashirakawa Oiwake-Cho, Kyoto 606-8502, Japan*

<sup>8</sup>*IPN Orsay, Université Paris Sud, IN2P3 – CNRS, F-91406 Orsay Cedex, France*

(Dated: October 29, 2020)

The properties of nuclei with extreme neutron-to-proton ratios, far from those naturally occurring on Earth, are key to understand nuclear forces and how nucleons hold together to form nuclei.  ${}^7\text{H}$ , with six neutrons and a single proton, is the nuclear system with the most unbalanced neutron-to-proton ratio known so far. However, its sheer existence and properties are still a challenge for experimental efforts and theoretical models. Here we report the formation of  ${}^7\text{H}$  as a resonance, detected with independent observables, and the first measurement of the structure and basic characteristics of its ground state. It is found that  ${}^7\text{H}$  is arranged as a  ${}^3\text{H}$  core surrounded by an extended four-neutron halo, with a unique four-neutron decay and a relatively long half-life thanks to neutron pairing. These properties are a prime example of new phenomena occurring in the most pure-neutron nuclear matter we can access in the laboratory.

Experimentally, the use of nuclear reactions with unstable nuclei permits to explore regions of the nuclear chart far from stability and beyond the limits of particle binding by systematically adding or removing nucleons [1]. This is particularly feasible for light nuclei, where the binding limits and large neutron-to-proton ratios can be reached by adding few nucleons to stable isotopes. In hydrogen, experiments have already obtained evidences of  ${}^4,{}^5,{}^6,{}^7\text{H}$  isotopes in a chain of four resonances beyond the neutron dripline [2–7]. These systems are found to decay by neutron emission and thus believed to be built on a core of  ${}^3\text{H}$  surrounded by neutrons contained by a centrifugal barrier and grouped in pairs. The systematic study of such a chain helps to understand the evolution of nuclear phenomena, as the effect of neutron pairing and the properties of dilute nuclear matter [8], away from

stability and into the nuclear continuum. At the end of this chain we find the super-heavy  ${}^7\text{H}$  isotope, the nucleus with the most unbalanced neutron-to-proton ratio of the nuclear chart.  ${}^7\text{H}$  is expected to display unique characteristics and open questions. Neutron pairing may render  ${}^7\text{H}$  the least unstable of the chain despite being the most neutron-rich [9–11], forcing it to decay directly to  ${}^3\text{H}$  by emitting four neutrons simultaneously. Concerning its structure, a recent model based on Antisymmetrised Molecular Dynamics (AMD) describes  ${}^7\text{H}$  as a di-neutron condensate with its four outer neutrons grouped in pairs, acting as two bosons held together by their interaction with a  ${}^3\text{H}$  core [10]. This model also predicts the halo of  ${}^7\text{H}$  to extend up to 4 fm, which corresponds to a nuclear density below  $0.014\text{ fm}^{-3}$ , more than 10 times lower than the saturation density of nuclear matter. These conditions of density and extreme neutron-to-proton ratio are unique in a nuclear system that can be studied in the laboratory and similar to those expected in a neutron-star crust [12, 13].

From the experimental point of view, the access to these nuclear systems is challenging: their production probabilities are very small; their short lifetimes, of the order of  $10^{-22}$  s, prevent direct measurements; and their multi-particle decays complicate the identification of the resonances. This is particularly true for  ${}^7\text{H}$ , with very few experiments with low statistics reporting evidences on its formation. Meanwhile, its main characteristics, even its existence, are yet to be precisely determined. Depending on the experiment, the

---

\* manuel.fresco@usc.es

† roger@ganil.fr

‡ Current affiliation: Department of Physics, University of Regina, Regina, SK S4S 0A2, Canada

§ Current affiliation: Indian Institute of Technology (Indian School of Mines), Dhanbad, Jharkhand - 826004, India

¶ Current affiliation: LPC Caen, Université de Caen Basse-Normandie–ENSICAEN–CNRS/IN2P3, F-14050 Caen Cedex, France

\*\* Current affiliation: Canadian Nuclear Laboratories, Canada

†† Current affiliation: GANIL, CEA/DSM–CNRS/IN2P3, BP 55027, F-14076 Caen Cedex 5, France

‡‡ Current affiliation: Irfu, CEA, Université Paris–Saclay, 91191 Gif-sur-Yvette, France

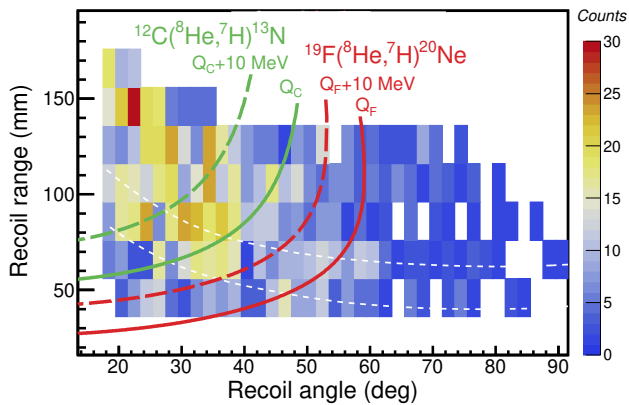


FIG. 1. Kinematics of target-like recoil. The figure shows the range of target-like products as a function of their recoil angle for events measured in coincidence with the identification of a  ${}^3\text{H}$  in the dE-E telescope. The colour lines show the kinematics for two reference Q-values of one-proton transfer with  ${}^{19}\text{F}$  (red) and  ${}^{12}\text{C}$  (green). The white dashed lines enclose the data displayed in Fig. 2.

${}^7\text{H}$  mass was estimated between 0.6 and 2 MeV above the  ${}^3\text{H}+4n$  mass, with a resonance width between  $\sim 0.1$  and 2 MeV [6, 14, 15]; and even excited states were reported at  $\sim 6$  MeV [14]. As to its structure, there is no experimental data on the  ${}^7\text{H}$  spin and parity.

In order to contribute to these sparse results, we have explored binary, one-proton transfer reactions between a  ${}^8\text{He}$  beam at 15.4A MeV and carbon and fluorine targets to produce and characterise the  ${}^7\text{H}$  ground state with the MAYA active-target [16] and the CATS beam-tracking detectors [17] at GANIL (France). The MAYA active-target detector works essentially as a Time, Charge-Projection Chamber where the filling gas, in this case  $\text{He}+\text{CF}_4$ , also plays the role of reaction target. In a proton-transfer event producing  ${}^7\text{H}$ , the incident  ${}^8\text{He}$  beam interacts with either a  ${}^{12}\text{C}$  or  ${}^{19}\text{F}$  nucleus and yields a  ${}^{13}\text{N}$  or  ${}^{20}\text{Ne}$  target-like recoil that is stopped inside MAYA, where its range, angle, and deposited energy are measured. Less than  $10^{-20}$  s after the reaction, the  ${}^7\text{H}$  beam-like product decays into a  ${}^3\text{H}$  nucleus, which is measured in an array of ancillary detectors, and four neutrons that escape undetected. We identify the transfer of one proton to  ${}^{19}\text{F}$  or  ${}^{12}\text{C}$  by using the relation between the angle and range of the target-like recoils, which is unique for each binary reaction channel. Figure 1 shows this correlation for the measured data, along reference kinematic lines for one-proton transfer reactions with  ${}^{12}\text{C}$  and  ${}^{19}\text{F}$ . In the calculation of these kinematics, the mass of  ${}^7\text{H}$  is taken as the sum of  ${}^3\text{H}$  and four neutrons, and the corresponding reaction Q-values are  $Q_{\text{F}}=-10.07$  MeV for  ${}^{19}\text{F}$  and  $Q_{\text{C}}=-20.97$  MeV for  ${}^{12}\text{C}$ . The accumulation

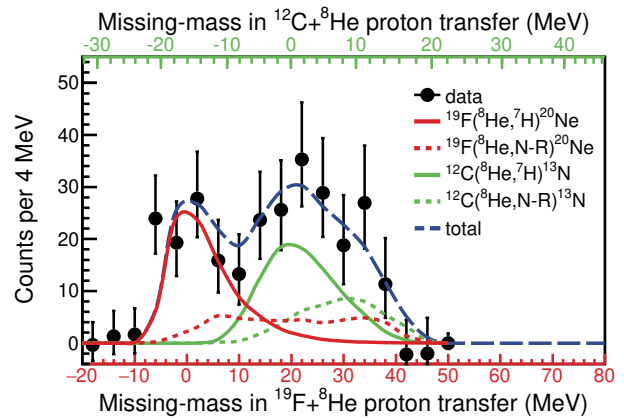


FIG. 2. Observation of the  ${}^7\text{H}$  resonance. The data selected between the white dashed lines in Fig. 1 (black dots) is shown in the missing-mass distributions of the beam-like products, calculated in one-proton transfer reactions with  ${}^{19}\text{F}$  (red bottom axis) or  ${}^{12}\text{C}$  (green top axis) targets, after subtraction of background from incomplete events (see Methods). Error bars correspond to one standard deviation of statistical uncertainty. The double-humped structure is reproduced by the production of  ${}^7\text{H}$  (solid lines) on top of non-resonant backgrounds (N-R, dashed lines) from reactions with  ${}^{19}\text{F}$  and  ${}^{12}\text{C}$  targets (red and green lines, respectively).

of events around the kinematic lines of  $Q_{\text{F}}$  and  $Q_{\text{C}}$  in Fig. 1 is a first indication of the production of  ${}^7\text{H}$  in both channels.

Since  ${}^7\text{H}$  decays immediately after being formed, its characteristics are indirectly measured with the missing-mass method, in which the mass of the undetected participant ( ${}^7\text{H}$ , in this case) is deduced from the energy and momenta of the remaining participants in the reaction (incident  ${}^8\text{He}$ , target  ${}^{19}\text{F}/{}^{12}\text{C}$ , and recoil  ${}^{20}\text{Ne}/{}^{13}\text{N}$ ). Figure 2 shows the missing-mass spectrum of the beam-like product from one-proton transfer reactions with respect to the mass of the  ${}^3\text{H}+4n$  subsystem for data between the white dashed lines of Fig. 1. Our experimental setup does not perform element separation of the target-like recoils, thus the figure shows the missing-mass as calculated for each  ${}^{19}\text{F}$  and  ${}^{12}\text{C}$  targets. The events accumulated around the  $Q_{\text{F}}$  and  $Q_{\text{C}}$  kinematic lines shown in Fig. 1 appear in Fig. 2 as two peaks: one around zero in the missing-mass spectra of  ${}^{19}\text{F}$  targets and another around zero for  ${}^{12}\text{C}$  targets. The first peak lies in a clean kinematical region of the  ${}^{19}\text{F}$  missing-mass; only low-lying states of  ${}^7\text{H}$  or the lower tail of a 3-body non-resonant continuum (which would not be a peak) can populate it. Other channels, such as breakup channels, are subtracted from our selections. We can safely assign this peak to the formation of  ${}^7\text{H}$  with  ${}^{19}\text{F}$  targets. The second peak occupies a region that can be populated not only by the production of  ${}^7\text{H}$  with  ${}^{12}\text{C}$  but also by other multi-particle transfer channels. A fit to possible contri-

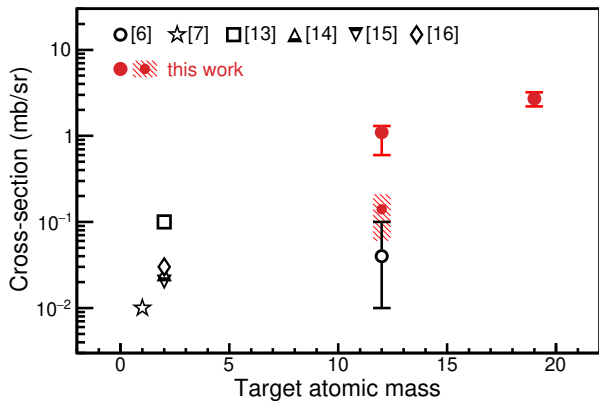


FIG. 3. Differential cross-section of  ${}^7\text{H}$  production as a function of the target atomic mass. Black open symbols correspond to previous measurements [6, 7, 14, 15, 18, 19]. Red solid symbols are one-proton transfers with  ${}^{12}\text{C}$  and  ${}^{19}\text{F}$  from this work. The shaded red dot shows our data evaluated in the same angular region of ref. [6], with the shaded area its uncertainty. Error bars are shown only when reported in the source reference and correspond to one standard deviation.

butions other than  ${}^7\text{H}$  and its non-resonant continuum sets an upper limit of  $\sim 0.2$  mb/sr to their production (see Methods for a detailed account on the influence of other channels in our data analysis).

The values of the resonance mass and width are obtained by fitting a simulation of the main experimental observables to the collected data. This simulation includes the production of the resonance and non-resonant contributions in both  ${}^{12}\text{C}$  and  ${}^{19}\text{F}$  targets, folded with the experimental uncertainty and measurement conditions. The measured distributions, and in particular the observed widths, are dominated by the experimental uncertainty, which can reach  $\sim 10$  MeV depending on the kinematical region and determines the final uncertainty on the measurement of the resonance parameters.

The results of the fit describe a low-lying, narrow resonance state with a mass of  $0.73^{+0.58}_{-0.47}$  MeV above the  ${}^3\text{H}+4\text{n}$  mass and a width of  $0.18^{+0.47}_{-0.16}$  MeV. The mass value confirms  ${}^7\text{H}$  as the least unstable of the known hydrogen resonances, less than 1 MeV close to being bound, despite being the most neutron-rich. A similar behaviour is found in the neighbouring helium chain [9], where the nucleon pairing makes the binding energy of extra neutrons added to a  ${}^4\text{He}$  core also minimum in  ${}^8\text{He}$ , with two neutron pairs in the p-shell. Assuming an equivalent evolution for the hydrogen resonances, one can expect  ${}^7\text{H}$  to be the least unstable of the whole chain, including possible  ${}^8,9\text{H}$  resonances. The reinforced stability brought by neutron pairing also gives a narrow width to  ${}^7\text{H}$ , which translates into a half-life of  $\sim 5 \cdot 10^{-21}$  s, an order of magnitude longer than the other hydrogen resonances.

Compared to previous experiments, our measured

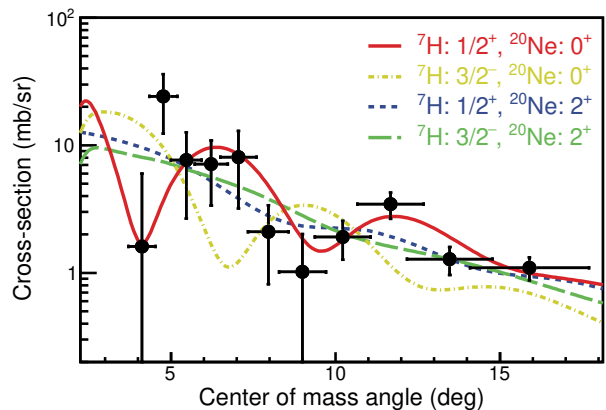


FIG. 4. Differential cross-section of the  ${}^{19}\text{F}+{}^8\text{He}$  proton-transfer channel. The shape of the angular distribution (black dots) is well reproduced by a DWBA calculation of a proton transfer to a  $1/2^+$  state in  ${}^7\text{H}$  and a  ${}^{20}\text{Ne}$  in its  $0^+$  ground state (red line). Other spin combinations (yellow, green, and blue lines) do not follow the measured data. Vertical error bars include statistical uncertainty and the effect of the uncertainty in the parameters of the resonance, while horizontal error bars show the uncertainty in the calculation of the c.m. angle. Both correspond to one standard deviation.

mass and width are in good agreement with the  $0.57^{+0.42}_{-0.21}$  and  $0.09^{+0.94}_{-0.06}$  MeV reported in ref. [6], and the mass is similar to the  $1.8 \pm 0.5$  MeV estimated in ref. [14]. Evidences of excited states of  ${}^7\text{H}$  around 6 MeV were also reported in ref. [14]. In the case of the  ${}^{19}\text{F}$  channel, these states may be hidden in the tail of the peak associated with the  ${}^7\text{H}$  ground state. A fit to a tentative state around 6 MeV gives no statistically significant population within the uncertainties. We estimate that our data would be sensitive to such population above 0.1 mb/sr. From the theory side, calculations tend to overestimate the  ${}^7\text{H}$  mass. In particular, models based on a di-neutron condensate from AMD [11] and on hyperspherical functions methods [9] describe a resonance with a mass of  $\sim 3$  MeV [10]. Concerning the resonance width, ref. [11] finds a strong correlation with the resonance mass and it predicts values below 1 keV for masses around 1 MeV, two orders of magnitude below the measured width.

The capabilities of MAYA to measure low energy products and the relatively high intensity of the  ${}^8\text{He}$  beam have allowed us to collect more than 200 events assigned to  ${}^7\text{H}$  formation. The average production cross-section with  ${}^{19}\text{F}$  is  $2.7 \pm 0.5$  mb/sr between  $4^\circ$  and  $18^\circ$  in the centre of mass reference frame (c.m.), whereas  ${}^{12}\text{C}$  yields  $1.1^{+0.2}_{-0.5}$  mb/sr between  $5^\circ$  and  $30^\circ$ . The  ${}^{12}\text{C}$  channel was also measured in ref. [6], reporting  $0.04^{+0.06}_{-0.03}$  mb/sr between  $10^\circ$  and  $48^\circ$ . When evaluated in the same angular region, our measurement averages to  $0.14^{+0.07}_{-0.08}$  mb/sr,

a larger, although compatible, value. Concerning other transfer measurements, refs. [14, 15, 18, 19] find values below 0.1 mb/sr with deuterium targets and, in general, higher beam energies. In addition to these transfer measurements, the cross-section from proton knock-out in the pioneering work of ref. [7] decreases in another order of magnitude. While a precise comparison between these values is difficult due to the different angular coverage and low statistics, we can observe in Fig. 3 a clear effect from the target of choice: the cross-section increases with increasing target size. From the theoretical point of view, Distorted-Wave Born Approximation (DWBA) calculations made with the coupled-channels FRESKO program [20] are found to be very sensitive to the descriptions of the participants in the reaction, and predict a cross-section that can vary between a factor 4 and 12 below our data with respect to small variations to the  $^8\text{He}$  density. Nonetheless, the underestimation of the cross-section suggests that there is margin to improve the theoretical description of the reaction mechanism leading to the formation of  $^7\text{H}$ .

The improved statistics have also permitted to measure the angular distribution, i.e., the probability of producing  $^7\text{H}$  as a function of the c.m. angle. Figure 4 shows that the angular distribution of the  $^{19}\text{F}(^8\text{He}, ^7\text{H})^{20}\text{Ne}$  channel follows a clear oscillating pattern, with distinct minima. This behaviour is a strong indication of the formation of two well-defined systems in the output channel:  $^{20}\text{Ne}$  and the  $^7\text{H}$  resonance; it offers a further, independent confirmation of its production. The angular distribution is compared in Fig. 4 with different DWBA calculations made with the FRESKO code and scaled to the experimental data. The resonance nuclear density was obtained from AMD calculations assuming a di-neutron condensate structure around a  $^3\text{H}$  core [10]. We explore the possibility of populating the  $0^+$  ground state or the  $2^+$  first excited state of  $^{20}\text{Ne}$ , and for  $^7\text{H}$ , we consider either a  $1/2^+$  state with a  $^3\text{H}$  core in its ground state and four outer neutrons, or a  $3/2^-$  state with an excited  $^3\text{H}$  core. The relative amplitude of the oscillations and the positions of the minima are best reproduced with a proton transfer to the  $0^+$  ground state of  $^{20}\text{Ne}$  and a  $1/2^+$   $^7\text{H}$  resonance. We can also see a slight systematic offset of  $\sim 0.5^\circ$  between the AMD calculations and our data. Since the positions of the minima are also driven by the sizes of the participants, this offset suggests that the outer neutron shell of  $^7\text{H}$  spreads even beyond 4 fm, with the neutron pairs in the halo separated in more than the 6 fm predicted by the AMD model [10]. The separation between the neutron pairs would hinder the formation of a four-neutron cluster within  $^7\text{H}$ , which may be of relevance for the ongoing search of a tetra-neutron resonance [21, 22].

In conclusion, we have measured the formation of the  $^7\text{H}$  resonance with statistical significance via two differ-

ent reaction channels and performed the characterisation of its ground state with two independent observables: the resonance missing-mass distribution and the angular distribution. From these observables, we have obtained a new determination of the mass and width of  $^7\text{H}$ , and, for the first time, the assignment of spin and parity to its ground state. Together, these results depict the super-heavy  $^7\text{H}$  nucleus as an extended pure-neutron shell around a  $^3\text{H}$  core in a  $1/2^+$  ground state. However, the same neutron pairing that allows this large neutron configuration also renders the  $^7\text{H}$  nucleus a long-lived and almost-bound resonance, despite being the system with the largest neutron-to-proton ratio in the nuclear chart known today.

## METHODS

### Experimental details and detectors

A  $^8\text{He}$  beam of  $10^4$  particles per second was produced and re-accelerated up to 15.4A MeV in the SPIRAL facilities at GANIL. MAYA was filled with 176 mbar of a 90%–10% molar mix of helium and  $\text{CF}_4$ . The  $^{19}\text{F}$  and  $^{12}\text{C}$  atoms contained in the filling gas acted as reaction targets with equivalent thickness of  $4.2 \cdot 10^{19}$  atoms/cm<sup>2</sup> of fluorine and  $1.1 \cdot 10^{19}$  atoms/cm<sup>2</sup> of carbon. Figure 5 shows a schematic drawing of the experimental setup with a typical  $^{19}\text{F}(^8\text{He}, ^7\text{H})^{20}\text{Ne}$  transfer event. The trajectory of the  $^8\text{He}$  projectile is measured by the CATS beam-tracking detectors before entering MAYA. Once inside, the  $^8\text{He}$  projectile interacts with a  $^{19}\text{F}$  nucleus contained in the  $\text{CF}_4$  gas and transfers a proton, yielding a  $^{20}\text{Ne}$  nucleus and a  $^7\text{H}$  resonance that immediately decays into  $^3\text{H}$  and four neutrons. The trajectory of the target-like  $^{20}\text{Ne}$  is imaged by induced charges on the segmented pad plane of MAYA and the angle and range are measured with typical uncertainties of  $1.2^\circ$  and 16 mm, respectively. The  $^3\text{H}$  scattered at forward angles is identified in a dE–E telescope composed of a first layer of  $20 \cdot 5 \times 5\text{-cm}^2$ ,  $75\text{-}\mu\text{m}$  thick silicon detectors and a second layer of  $80 \cdot 2.5 \times 2.5 \text{ cm}^2$ , 1-cm thick CsI crystal detectors. In this setup, neutrons are not detected. Similarly,  $^{12}\text{C}(^8\text{He}, ^7\text{H})^{13}\text{N}$  reactions also occur with the  $^{12}\text{C}$  present in the  $\text{CF}_4$  gas. Unreacted beam projectiles are collected before the dE–E telescope in a  $2 \times 2 \text{ cm}^2$  aluminium beam-stopper.

Two components of the measurement efficiency in MAYA are considered: the geometric efficiency and the efficiency of the reconstruction of the trajectories in the segmented cathode. The geometric efficiency accounts for losses due to steep azimuthal angles and for the effective target length, and it varies smoothly from  $\sim 90\%$  at  $90^\circ$  to  $\sim 40\%$  close to  $20^\circ$  in recoil angle. The reconstruction efficiency is 91% for events with a single  $^3\text{H}$  detected in the dE–E telescope. Concerning the beam-tracker de-

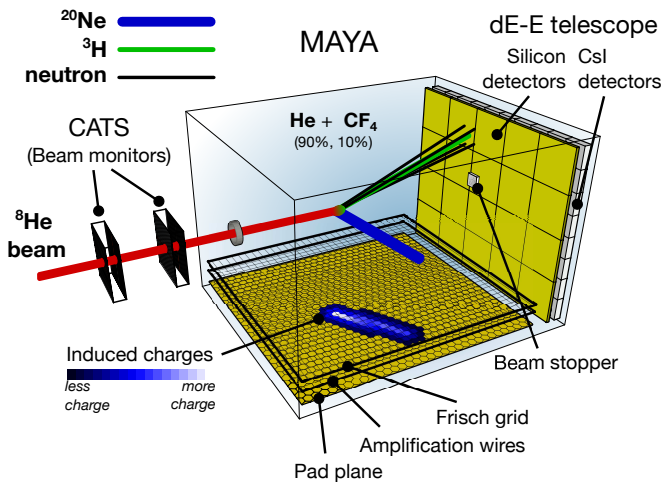


FIG. 5. Schematic drawing of the detection set-up. A typical proton-transfer reaction producing  ${}^7\text{H}$  with a  ${}^{19}\text{F}$  nucleus is also shown.

tectors, the efficiency of the CATS detectors ensemble was measured at 70%.

#### Identification of ${}^7\text{H}$ resonance production and separation from other reaction channels

The selection of  ${}^7\text{H}$  candidate events is done with the simultaneous measurement of both charged reaction products. A binary, proton-transfer reaction with  ${}^{12}\text{C}$  or  ${}^{19}\text{F}$  produces a single  ${}^3\text{H}$  detected in the dE-E telescope in coincidence with a single trajectory from the target-recoil product, projected on the pad plane. This selection rejects reactions with the helium atoms in the gas, where none of the products ionises enough to induce an image on the pad plane. The probability of random coincidences leading to a false correspondence between a measured  ${}^3\text{H}$  from one event and a recorded track from another, independent event is below 0.1%.

Fusion and high excitation breakup channels with more than two ionising products and/or more than two products on the dE-E telescope are also rejected. However, some breakup events may mimic one-proton transfer if only a  ${}^3\text{H}$  is detected in the dE-E telescope and a track is recorded in MAYA while the rest of the products are missed. The distribution of these incomplete events is obtained from those detected with a  ${}^3\text{H}$  in coincidence with any other product in the dE-E telescope and a track inside MAYA. The resulting distribution is subtracted from the set of  ${}^7\text{H}$  candidate events. This contamination of breakup channels amounts to less than 10% of single  ${}^3\text{H}$  and track events, and it follows a smooth behaviour without peaks or recognisable features.

Since we do not have isotopic identification of the recoil product, possible multi-particle transfer channels yield-

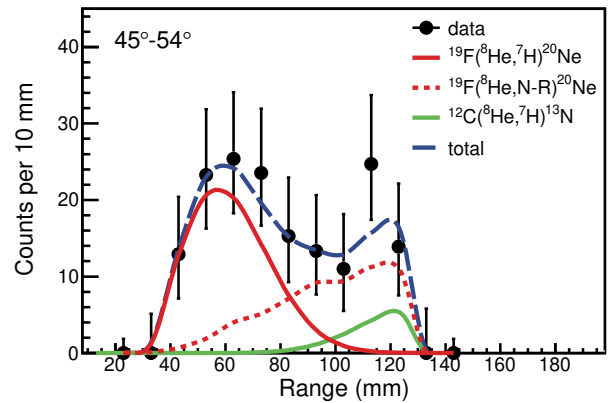


FIG. 6. Range distribution of target-like recoils. Black dots show the measured range distribution of target-like products from Fig. 1, with a recoil angle between  $45^\circ$  and  $54^\circ$  in the laboratory frame and after subtraction of background from incomplete events (see text). Error bars correspond to one standard deviation of statistical uncertainty. Solid lines correspond to the simulated distribution of the formation  ${}^7\text{H}$  with  ${}^{19}\text{F}$  (red) and  ${}^{12}\text{C}$  (green) targets. The dashed red line shows the non-resonant background (N-R) and the long-dashed blue line is the sum of all simulated distributions.

ing excited  ${}^7\text{H}$  and  ${}^{6,5}\text{H}$  resonances are addressed according their kinematics. When produced with  ${}^{19}\text{F}$  targets, their peaks are localised between  $\sim 6$  and  $20$  MeV in missing-mass. The fit to experimental data sets an upper limit to the production of excited  ${}^7\text{H}$  and  ${}^6\text{H}$  below  $\sim 0.1$  mb/sr, consistent with DWBA calculations and previous experiments. Below  $6$  MeV, the production of  ${}^7\text{H}$  with  ${}^{19}\text{F}$  targets is largely free of any contaminant. The production of  ${}^5\text{H}$  from  ${}^{19}\text{F}$  and  ${}^{6,5}\text{H}$  from  ${}^{12}\text{C}$  lies within the kinematical region of the production of  ${}^7\text{H}$  with  ${}^{12}\text{C}$ . For these channels, a conservative upper limit of  $\sim 0.2$  mb/sr can be set, also consistent with DWBA calculations and previous experiments [23]. The systematic uncertainty in the  ${}^7\text{H}$  production with  ${}^{12}\text{C}$  targets accounts for possible contamination from these underlying channels.

Finally, the fact that we reconstruct the missing-mass with the kinematics of the target-like recoil prevents our measurement to be affected by final-state interactions [24]. While these are probably present among the emitted  ${}^3\text{H}$  and neutrons, the angle between the trajectories of the target-like and beam-like products, and their large mass difference make the effect of final-state interactions negligible in our results.

#### Simulation and resonance parameters

In order to characterise the resonance [23], we have performed a simulation to produce the distribution of experimental observables of the relevant channels, folded with

the experimental resolutions and geometrical characteristics of the setup. The simulation includes the production of  ${}^7\text{H}$  with both  ${}^{19}\text{F}$  and  ${}^{12}\text{C}$  targets, and also non-resonant events. The latter are collisions where, even if a proton transfer has occurred, the resonance is not formed and more than two particles are produced in a single step. In this work, we have considered three possible phase-space components: 6-body ( ${}^{20}\text{Ne}+{}^3\text{H}+n+n+n+n$ ), 4-body ( ${}^{20}\text{Ne}+{}^3\text{H}+2n+2n$ ), and 3-body ( ${}^{20}\text{Ne}+{}^3\text{H}+4n$ ) partitions. Besides these channels, other multi-particle transfer reactions leading to other hydrogen resonances, such as deuteron or triton transfer from  ${}^8\text{He}$ , were also considered.

In order to describe the  ${}^7\text{H}$  system, we use a Breit–Wigner probability distribution with the form:

$$\sigma_{7\text{H}}(m) = \sigma_0 \frac{\Gamma_{7\text{H}} \sqrt{\frac{m}{m_{7\text{H}}}}}{(m_{7\text{H}} - m)^2 + \frac{1}{4} \left( \Gamma_{7\text{H}} \sqrt{\frac{m}{m_{7\text{H}}}} \right)^2}, \quad (1)$$

where  $m$  is the difference between the missing-mass of the beam-like product and the mass of the  ${}^3\text{H}+4n$  subsystem;  $\Gamma_{7\text{H}}$  is the width of the resonance,  $m_{7\text{H}}$  is its mass with respect to the mass of  ${}^3\text{H}+4n$ , and  $\sigma_0$  is a scaling factor. The squared root of the  $m/m_{7\text{H}}$  ratio accounts for the dependence of the neutron centrifugal barrier.

The mass and width of the resonance, as well as the scaling factor, were treated as free parameters and extracted from a log-likelihood minimisation between the simulation and the measured range distribution in the angular region between  $45^\circ$  and  $54^\circ$ , corresponding to  $10.9\text{--}17.4^\circ$  in the c.m. of  ${}^{19}\text{F}({}^8\text{He}, {}^7\text{H}){}^{20}\text{Ne}$ , shown in Fig. 6. This region is mainly populated by the production of  ${}^7\text{H}$  and non-resonant components, with a small contribution from the  ${}^{12}\text{C}({}^8\text{He}, {}^7\text{H}){}^{13}\text{N}$  channel, making it especially well-suited for a clean fit.

#### Angular distribution measurement and comparison with theory

The angular distribution was obtained with the log-likelihood fitting of the simulated range distributions to the measured data, corrected by the reconstruction and geometrical efficiency in MAYA. These fits were performed for  $3^\circ$ -wide slices of the recoil angle in the laboratory reference frame between  $21^\circ$  and  $54^\circ$ . For each angle slice, the number of events of each channel was obtained from the total integral of the corresponding simulated range distributions. In order to obtain the differential cross-section, each integral was normalised to the number of incoming  ${}^8\text{He}$  projectiles and atoms of  ${}^{19}\text{F}$  or  ${}^{12}\text{C}$  in the filling gas, and to the c.m. solid angle covered in each  $3^\circ$ -wide slice.

Systematic uncertainties from the number of incoming projectiles and target thickness are 0.7% of the measured

cross-section. The uncertainty on the position and width of the resonance also affects the integral of the simulated distributions and they contribute with a  $\sim 10\%$  of the final uncertainty of the angular distribution. The angular distribution of the  ${}^{12}\text{C}({}^8\text{He}, {}^7\text{H}){}^{13}\text{N}$  channel was also measured, although it suffered from large fluctuations, and large measured statistical and systematic uncertainties due to the contribution of competing channels, as discussed in the previous section. Its study does not allow a clear assignment of spin and parity but only an assessment of the mean differential cross-section.

The corresponding optical potentials used for the DWBA calculations of the theoretical cross-section were tested against the elastic  ${}^8\text{He}+{}^{19}\text{F}$  and  ${}^8\text{He}+{}^{12}\text{C}$  measured cross-sections. The production cross-sections calculated with FRESKO were obtained with shell-model spectroscopic factors for the  $\langle {}^{20}\text{Ne} | {}^{19}\text{F} \rangle$  overlaps, using the WBT effective interaction by Warburton and Brown [25]. Concerning  ${}^8\text{He}$  and  ${}^7\text{H}$ , we have explored the impact of different descriptions of the  ${}^8\text{He}$  density found in the literature and two densities for the  ${}^7\text{H}$  from the AMD model. The resulting cross-sections were folded with the experimental uncertainties and further scaled to match the experimental data. The scaling factor was found to be very sensitive to the nuclear densities of the participants. In particular, it can vary from  $4.5 \pm 2.8$  with a  ${}^8\text{He}$  matter radius of  $\text{RMS} = 2.37 \text{ fm}$  to  $12.7 \pm 6.1$  with  $\text{RMS} = 2.97 \text{ fm}$ . The density of the  ${}^7\text{H}$  seems have a reduced impact in the final result. Concerning channel mixing, a tentative fit to evaluate a possible mixture of transfer to  $0^+$  and  $2^+$  states in  ${}^{20}\text{Ne}$  gives a probability of less than 10% towards excited  $2^+$  states in  ${}^{20}\text{Ne}$ .

#### DATA AVAILABILITY

The data that support the findings of this study are available from the corresponding author upon reasonable request.

#### CODE AVAILABILITY

The codes and methods used to process and analyse the data presented in this paper are available from the corresponding author upon reasonable request.

#### ACKNOWLEDGMENTS

The authors thank Navin Alahari for the useful discussions and the careful reading of the manuscript, and Miguel Marqués for his help in the data analysis. The authors are deeply thankful to the technical staff at GANIL for their support and help. This work has been supported by the European Community

FP7–Capacities –Integrated Infrastructure Initiative– contract ENSAR n° 262010, and by the Spanish Ministerio de Economía y Competitividad under contracts FPA2009–14604–C02–01 and FPA2012–39404–C02–01. M.C. acknowledges the support by the Spanish Ministerio de Economía y Competitividad through the Programmes “Ramón y Cajal” with the grant number RYC–2012–11585 and “Juan de la Cierva” with the grant number JCI2009–05477.

#### AUTHOR CONTRIBUTIONS

M.C. and T.R. devised and coordinated the experiment, and performed the data analysis with contributions from B.F.–D.; A.M. and N.I. performed the theoretical calculations; M.C., T.R., G.F.G., J.P., S.B., S.S., and J.G. prepared and mounted the experimental setup; M.C., T.R., G.F.G., J.P., S.B., S.S., J.G., B.F.–D., J.B., D.C., F.F., B.J., D.P., B.P., R.R., D.R., C.R.–T., H.S. and M.V. participated on the data taking.

#### COMPETING INTERESTS

The authors declare no competing interests.

---

[1] P. G. Hansen, *Nature* **328**, 476 (1987).

[2] S. I. Sidorchuk *et al.*, *Phys. Lett. B* **594**, 54 (2004).

- [3] M. S. Golovkov *et al.*, *Phys. Lett. B* **566**, 70 (2003).  
 [4] A. H. Wuosmaa *et al.*, *Phys. Rev. C* **95**, 014310 (2017).  
 [5] A. V. Belozorov *et al.*, *Nucl. Phys. A* **460**, 352 (1986).  
 [6] M. Caamaño *et al.*, *Phys. Rev. Lett.* **99**, 062502 (2007).  
 [7] A. A. Korshennikov *et al.*, *Phys. Rev. Lett.* **90**, 082501 (2003).  
 [8] K. Hagino, H. Sagawa, J. Carbonell, and P. Schuck, *Phys. Rev. Lett.* **99**, 022506 (2007).  
 [9] N. K. Timofeyuk, *Phys. Rev. C* **65**, 064306 (2002); **69**, 034336 (2004).  
 [10] S. Aoyama and N. Itagaki, *Phys. Rev. C* **80**, 021304(R) (2009).  
 [11] M. S. Golovkov *et al.*, *Phys. Lett. B* **588**, 163 (2004).  
 [12] N. Chamel and P. Haensel, *Living Rev. Relativity* **11**, 10 (2008).  
 [13] F. Gulminelli and A. R. Raduta, *Phys. Rev. C* **92**, 055803 (2015).  
 [14] A. A. Bezbakh *et al.*, *Phys. Rev. Lett.* **124**, 022502 (2020).  
 [15] S. Fortier *et al.*, in *International Symposium on Exotic Nuclei*, AIP Conference Proceedings, Vol. 912 (2007) p. 3.  
 [16] C. E. Demonchy *et al.*, *Nucl. Instr. and Meth. A* **583**, 341 (2007).  
 [17] S. Ottini-Hustache *et al.*, *Nucl. Instr. and Meth. A* **431**, 475 (1999).  
 [18] G. M. Ter-Akopian *et al.*, *Eur. Phys. J. Special Topics* **150**, 61 (2007).  
 [19] E. Y. Nikolskii *et al.*, *Phys. Rev. C* **81**, 064606 (2010).  
 [20] I. J. Thompson, *Comp. Phys. Rep.* **7**, 167 (1988).  
 [21] F. M. Marqués *et al.*, *Phys. Rev. C* **65**, 044006 (2002).  
 [22] F. M. Marqués and Z. Yang, *RIKEN Accel. Prog. Rep.* **51**, 35 (2018).  
 [23] M. Caamaño *et al.*, *Phys. Rev. C* **78**, 044001 (2008).  
 [24] K. M. Watson, *Phys. Rev.* **88**, 1163 (1952).  
 [25] E. K. Warburton and B. A. Brown, *Phys. Rev. C* **46**, 923 (1992).

# Figures

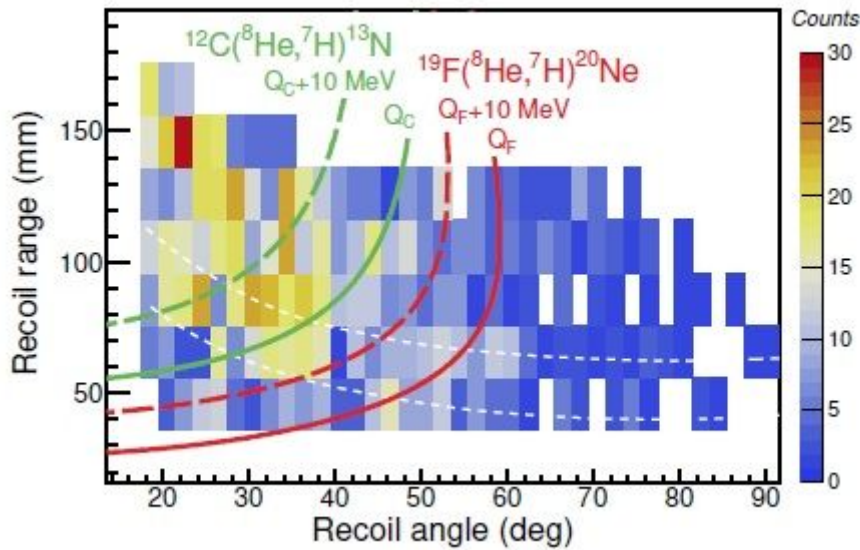


Figure 1

Kinematics of target-like recoil. The figure shows the range of target-like products as a function of their recoil angle for events measured in coincidence with the identification of a  $3\text{H}$  in the dE-E telescope. The colour lines show the kinematics for two reference Q-values of one-proton transfer with  $^{19}\text{F}$  (red) and  $^{12}\text{C}$  (green). The white dashed lines enclose the data displayed in Fig. 2.

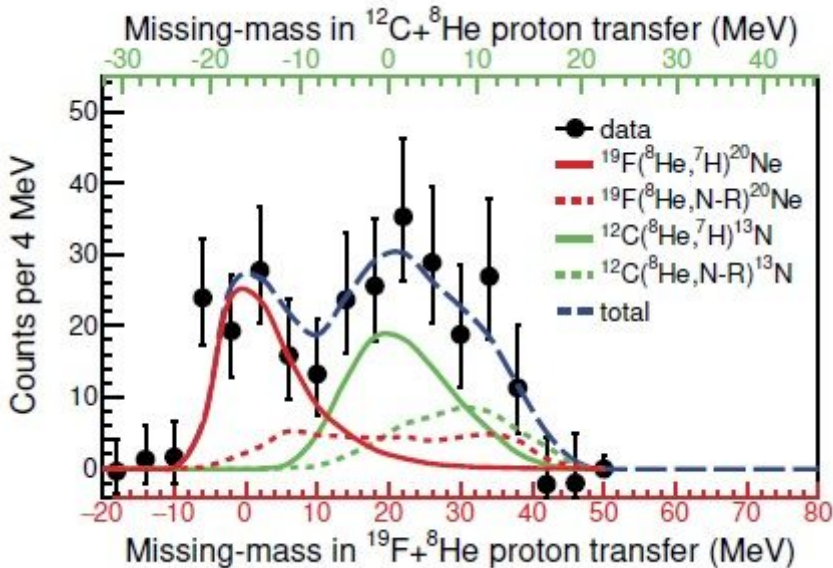
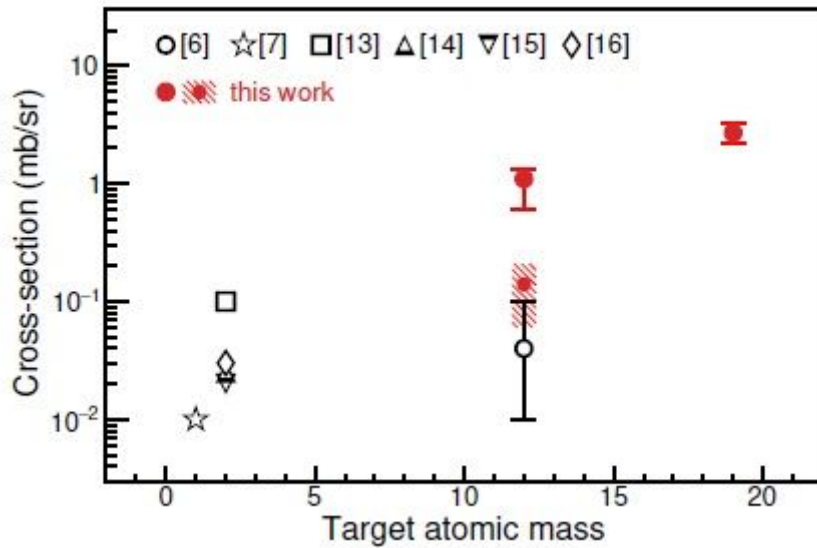


Figure 2

Observation of the  $7\text{H}$  resonance. The data selected between the white dashed lines in Fig. 1 (black dots) is shown in the missing-mass distributions of the beam-like products, calculated in one-proton transfer

reactions with  $^{19}\text{F}$  (red bottom axis) or  $^{12}\text{C}$  (green top axis) targets, after subtraction of background from incomplete events (see Methods). Error bars correspond to one standard deviation of statistical uncertainty. The double-humped structure is reproduced by the production of  $^7\text{H}$  (solid lines) on top of non-resonant backgrounds (N-R, dashed lines) from reactions with  $^{19}\text{F}$  and  $^{12}\text{C}$  targets (red and green lines, respectively).



**Figure 3**

Differential cross-section of  $^7\text{H}$  production as a function of the target atomic mass. Black open symbols correspond to previous measurements [6, 7, 14, 15, 18, 19]. Red solid symbols are one-proton transfers with  $^{12}\text{C}$  and  $^{19}\text{F}$  from this work. The shaded red dot shows our data evaluated in the same angular region of ref. [6], with the shaded area as its uncertainty. Error bars are shown only when reported in the source reference and correspond to one standard deviation.

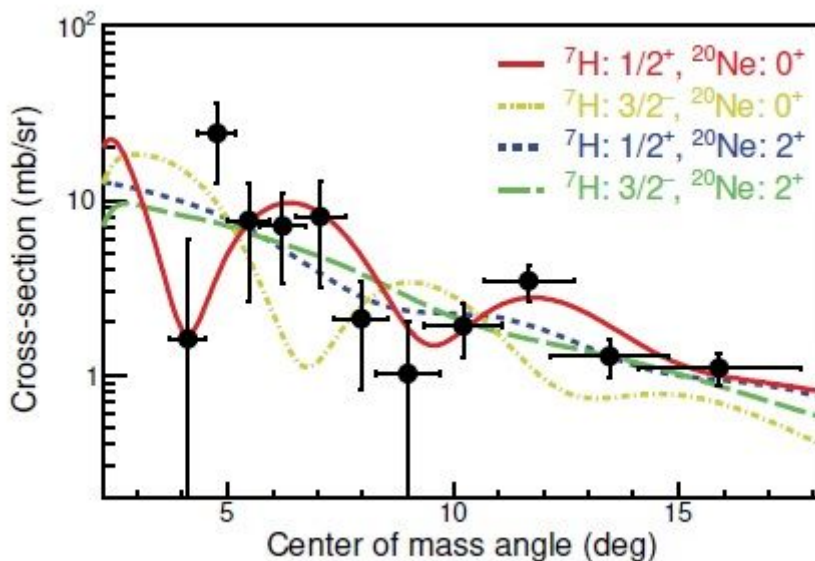


**Figure 4**

Differential cross-section of the  $^{19}\text{F}+^8\text{He}$  protontransfer channel. The shape of the angular distribution (black dots) is well reproduced by a DWBA calculation of a proton transfer to a  $1/2^+$  state in  $^7\text{H}$  and a  $^{20}\text{Ne}$  in its  $0^+$  ground state (red line). Other spin combinations (yellow, green, and blue lines) do not follow the measured data. Vertical error bars include statistical uncertainty and the effect of the uncertainty in the parameters of the resonance, while horizontal error bars show the uncertainty in the calculation of the c.m. angle. Both correspond to one standard deviation.

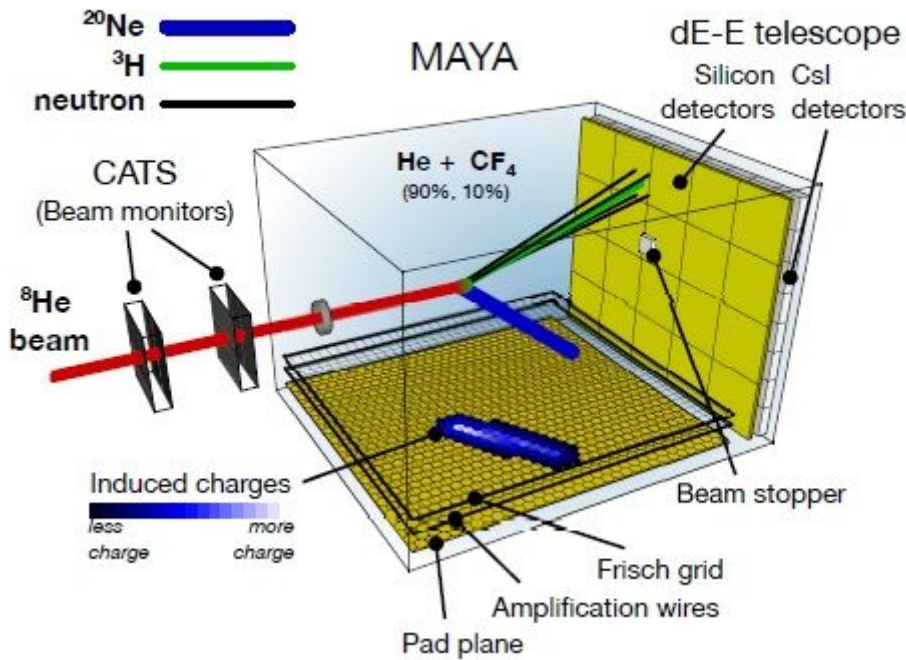
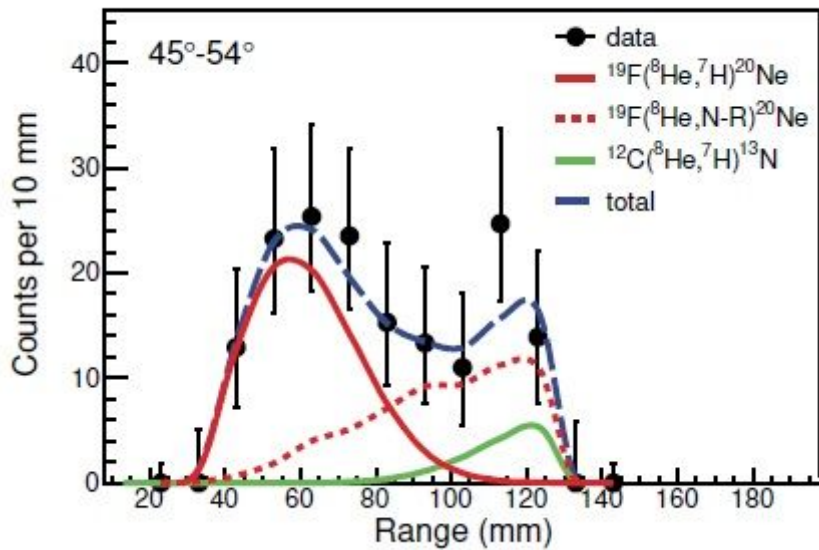


Figure 5

Schematic drawing of the detection set-up. A typical proton-transfer reaction producing  $^7\text{H}$  with a  $^{19}\text{F}$  nucleus is also shown.



**Figure 6**

Range distribution of target-like recoils. Black dots show the measured range distribution of target-like products from Fig. 1, with a recoil angle between  $45^\circ$  and  $54^\circ$  in the laboratory frame and after subtraction of background from incomplete events (see text). Error bars correspond to one standard deviation of statistical uncertainty. Solid lines correspond to the simulated distribution of the formation  $7\text{H}$  with  $^{19}\text{F}$  (red) and  $^{12}\text{C}$  (green) targets. The dashed red line shows the non-resonant background (N-R) and the long-dashed blue line is the sum of all simulated distributions.